Suspended silicon mid-infrared waveguide devices with subwavelength grating metamaterial cladding

J. Soler Penades,[1,*] A. Ortega-Moñux,[2] M. Nedeljkovic,[1] J. G. Wangüemert-Pérez,[2] R. Halir,[2] A.Z. Khokhar,[1] C. Alonso-Ramos,[3] Z. Qu,[1] I. Molina-Fernández,[2] P. Cheben[4] and G. Z. Mashanovich[1,5]

1 Optoelectronics Research Centre, University of Southampton, Southampton SO17 1BJ, United Kingdom
2 Universidad de Málaga, Dpto. de Ingeniería de Comunicaciones, ETSI Telecomunicación, Campus de Teatinos, 29071 Málaga, España
3 Centre de Nanosciences et de Nanotechnologies, CNRS, Univ. Paris-Sud, Université Paris-Saclay, 91405 Orsay cedex, France
4 National Research Council Canada, Building M-50, Ottawa, K1A 0R6 Canada
5 School of Electrical Engineering, University of Belgrade, 11120 Belgrade, Serbia
**jsp1a15@soton.ac.uk*

Abstract: We present several fundamental photonic building blocks based on suspended silicon waveguides supported by a lateral cladding comprising subwavelength grating metamaterial. We discuss the design, fabrication, and characterization of waveguide bends, multimode interference devices and Mach-Zehnder interferometers for the 3715 - 3800 nm wavelength range, demonstrated for the first time in this platform. The waveguide propagation loss of 0.82 dB/cm is reported, some of the lowest loss yet achieved in silicon waveguides for this wavelength range. These results establish a direct path to ultimately extending the operational wavelength range of silicon wire waveguides to the entire transparency window of silicon.

OCIS codes: (040.3060) Infrared; (130.0130) Integrated optics; (130.0250) Optoelectronics; (230.7370) Waveguides; (230.0230) Optical devices.

References and links

1. M. Nedeljkovic, A. Z. Khokhar, Y. Hu, X. Chen, J. Soler Penadés, S. Stankovic, H. M. H. Chong, D. J. Thomson, F. Y. Gardes, G. T. Reed, and G. Z. Mashanovich, "Silicon photonic devices and platforms for the mid-infrared, " Opt. Mater. Express **3**, 1205-1214 (2013).
2. R. Soref, "Mid-infrared photonics in silicon and germanium, "Nature Photon. **4**, 495-497 (2010).
3. T. Baehr-Jones, A. Spott, R. Ilic, A. Spott, B. Penkov, W. Asher, and M. Hochberg, "Silicon-on-sapphire integrated waveguides for the mid-infrared," Opt. Express **18**, 12127-12135 (2010).
4. J. Mu, R. Soref, L. C. Kimerling, and J. Michel, "Silicon-on-nitride structures for mid-infrared gap-plasmon waveguiding," Appl. Phys. Lett. **104**, 031115 (2014).
5. Y.-C. Chang, V. Paeder, L. Hvozdara, J.-M. Hartmann, and H. P. Herzig, "Low-loss germanium strip waveguides on silicon for the mid-infrared," Opt. Lett. **37**, 2883-2885 (2012).
6. M. Nedeljkovic, J. Soler Penadés, C. J. Mitchell, T. Dominquez Bucio, A. Z. Khokhar, C. Littlejohns, F. Y. Gardes, and G. Z. Mashanovich, "Surface grating coupled low loss Ge-on-Si rib waveguides and multimode interferometers," IEEE Photon. Technol. Lett. **27**, 1040-1043, (2015).
7. Z. Cheng, X. Chen, C. Y. Wong, K. Xu and H. K. Tsang, "Mid-infrared suspended membrane waveguide and ring resonator on silicon-on-insulator," IEEE Photon. J. **4,** 1510-1519 (2012).
8. Y. Xia, C. Qiu, X. Zhang, W. Gao, J. Shu, and Q. Xu, "Suspended Si ring resonator for mid-IR application, " Opt. Lett. **38**, 1122-1124 (2013).
9. J. Soler Penadés, C. Alonso-Ramos, A. Z. Khokhar, M. Nedeljkovic, L. A. Boodhoo, A. Ortega-Moñux, I. Molina-Fernández, P. Cheben, and G. Z. Mashanovich, "Suspended SOI waveguide with sub-wavelength grating cladding for mid-infrared," Opt. Lett. **39**, 5661-5664 (2014).
10. P. Cheben, P. J. Bock, J. H. Schmid, J. Lapointe, S. Janz, D.-X. Xu, A. Densmore, A. Delâge, B. Lamontagne, and T. J. Hall, "Refractive index engineering with subwavelength gratings for efficient microphotonic couplers and planar waveguide multiplexers," Opt. Lett. **35**, 2526-2528 (2010)
11. R. Halir, P. J. Bock, P. Cheben, A. Ortega-Moñux, C. Alonso-Ramos, J. H. Schmid, J. Lapointe, D.-X. Xu, J. G. Wangüemert-Pérez, Í. Molina-Fernández and S. Janz "Waveguide sub-wavelength structures: a review of principles and applications, " Laser Photonics Rev. **9**, 25–49 (2015).
12. M. Nedeljkovic, "Silicon photonic modulators for the mid-infrared," University of Southampton, Physical Sciences and Engineering, Doctoral Thesis (2013).

13. L. Zavargo-Peche, A. Ortega-Monux, J. G. Wanguemert-Perez, and I. Molina-Fernandez, "Fourier based combined techniques to design novel sub-wavelength optical integrated devices," Prog. Electromagn. Res. **123**, 447-465, (2012).
14. D. Kim, A. Barkai, R. Jones, N. Elek, H. Nguyen, and A. Liu, "Silicon-on-insulator eight-channel optical multiplexer based on a cascade of asymmetric Mach-Zehnder interferometers," Opt. Lett. **33**, 530–532 (2008).
15. R. Halir, G. Roelkens, A. Ortega-Moñux, and J. G. Wangüemert-Pérez, "High-performance 90° hybrid based on a silicon-on-insulator multimode interference coupler," Opt. Lett. **36**, 178–180 (2011).
16. R. Halir, I. Molina-Fernández, A. Ortega-Moñux, J. G. Wangüemert-Pérez, D.-X. Xu, P. Cheben, and S. Janz, "A design procedure for high performance, rib waveguide based multimode interference couplers in silicon-on-insulator," J. Lightwave Technol. **26**(16), 2928–2936 (2008).
17. A. Ortega-Moñux, L. Zavargo-Peche, A. Maese-Novo, I. Molina-Fernández, R. Halir, J. G. Wangüemert-Pérez, P. Cheben, and J. H. Schmid, "High-performance multimode interference coupler in silicon waveguides with subwavelength structures," IEEE Photon. Technol. Lett. **23**(19), 1406-1408, (2011).
18. Y. Zhang, A. Hosseini, X. Xu, D. Kwong, and R. T. Chen, "Ultralow-loss silicon waveguide crossing using Bloch modes in index-engineered cascaded multimode-interference couplers," Opt. Lett. **38**(18), 3608-3611 (2013).
19. L. B. Soldano and E. C. M. Pennings, "Optical multi-mode interference devices based on self-imaging: Principles and applications," J. Lightw. Technol. **13**(4), 615–627 (1995).
20. R. Halir, P. Cheben, S. Janz, D. Xu, Í. Molina-Fernández, and J. G. Wangüemert-Pérez, "Waveguide grating coupler with subwavelength microstructures," Opt. Lett. **34**, 1408-1410 (2009).
21. Z. Cheng, X. Chen, C. Y. Wong, K. Xu, C. K. Y. Fung, Y. M. Chen, and H. K. Tsang, "Focusing subwavelength grating coupler for mid-infrared suspended membrane waveguide," Opt. Lett. **37**(7), 1217–1219 (2012).
22. G. Z. Mashanovich et al., "Silicon photonic waveguides and devices for near- and mid-IR applications," IEEE J. Sel. Topics Quantum Electron. **21**(4), 407-418 (2015).

1. Introduction

Silicon-on-insulator (SOI) is the dominant platform for the implementation of integrated silicon photonic devices at near-infrared wavelengths. However, utilization of SOI in the mid-infrared (MIR) region is largely restricted due to buried oxide (BOX) layer absorption for wavelengths between 2.75 - 3.0 μm and beyond 4 μm [1, 2]. Therefore, other waveguide platforms are being exploited for the MIR applications, including silicon-on-sapphire [3], silicon-on-nitride [4] or germanium-on-silicon [5, 6]. An alternative approach relies on selective removal of the buried oxide in the SOI platform, yielding Si membrane waveguides. This way, SOI operational wavelength range can be expanded to cover the full Si transparency window up to 8 μm, yet benefiting from SOI mature fabrication processes. The buried oxide can be removed by using an array of holes etched along the sides of a rib waveguide, and then using hydrofluoric acid (HF) to etch the SiO_2 underneath the Si waveguide core [7,8]. Using this approach, propagation loss of 3 dB/cm at 2.75 μm wavelength was achieved [7]. However, this technique requires two etch steps, a shallow etch to define the rib waveguide and a full etch to form the lateral venting holes. In addition, a comparatively large distance between the rib waveguide and the fully etched holes, required to minimize mode perturbation, results in wide and thin Si membranes with limited mechanical stability. In [9], we presented a new type of mid-IR silicon membrane waveguide based on a single etch step process, with improved mechanical stability and measured propagation loss of 3.4 dB/cm at 3.8 μm wavelength. In this structure, light is guided in the Si strip defined between two periodic lattices of fully-etched holes which act as a subwavelength grating metamaterial cladding [see Fig. 1(a)]. The lattice periodicity is smaller than half of the effective wavelength in the waveguide, to supress diffraction effects. The resulting subwavelength grating metamaterial thereby behaves as an effective homogeneous medium with a refractive index (n_{swg}) intermediate between the indexes of silicon and air [10, 11]. Thus, the subwavelength grating (SWG) metamaterial acts as a low index region, forming a lateral cladding. At the same time, it provides access to the buried oxide for HF attack, while anchoring the waveguide to the Si slab to form the suspended membrane. By combining both the optical waveguiding and membrane suspending functions in the same SWG structure, the mid-IR silicon wire waveguides can be readily implemented using a single etch step. Furthermore, this approach helps in significantly reducing the width of the Si membrane, improving its mechanical stability.

Residual stress originating from high temperature fabrication process of SOI wafers is released once the silicon layer is separated from the buried oxide, resulting in Si membrane bending and compromising mechanical integrity. This effect is of particular concern when using wider suspended regions. Therefore, the SWG cladding design which performs well for narrow waveguides [9] is not suitable for suspending wider structures. This is an important practical limitation, since waveguide core widths of a few micrometers or more are required in different planar waveguide devices such as Multimode Interference (MMI) couplers and wavelength multiplexers with slab waveguide free-propagation region, to name a few.

In this work, we present several fundamental photonic functional blocks, building upon the concept of SWG engineered suspended MIR SOI waveguides. Specifically, we demonstrate for the first time compact and low loss 90º bends, S-bends, 2×2 multimode interference (MMI) couplers and Mach-Zehnder interferometers (MZIs). Furthermore, by optimizing waveguide geometry and fabrication process, we achieved a remarkably low waveguide propagation loss of 0.82 dB/cm at 3.8 µm wavelength.

Our devices have been implemented in an SOI with 500-nm-thick silicon and a 3-µm-thick buried oxide (BOX) layer. The design wavelength was set to 3.8 µm, for compatibility with the laser and detector system presently used in our measurement setup [12]. At this wavelength, the SiO_2 material absorption is approximately 5 dB/cm, resulting in a noticeable propagation loss penalty for conventional SOI waveguides [9]. All devices in this work were designed for TE (inplane) polarization using an in-house simulation tool, based on the Fourier Eigenmode Expansion Method (F-EEM) [13], which is particularly efficient for the analysis of periodic waveguide structures.

2. Design of suspended waveguide structures with SWG metamaterial cladding

2.1. Interconnecting waveguides

The geometry of the suspended waveguide with SWG cladding is schematically shown in Fig. 1. This structure comprises a solid silicon waveguide core of width W_{core} and a lateral SWG metamaterial cladding of width W_{clad}. The SWG cladding is implemented as a *z*-periodic array of rectangular air holes of length separated by Si stripes of length L_{Si}, i.e. the SWG pitch is $\Lambda = L_{hole} + L_{Si}$. The lateral SWG metamaterial cladding performs three different functions: i) it provides the lateral refractive index contrast required for optical waveguiding, ii) it allows the flow of the hydrofluoric acid (HF) to remove the buried oxide, and iii) it mechanically supports the Si waveguide core connecting it to the un-etched Si slab. In order to efficiently implement these functionalities, our design includes the following fundamental considerations:

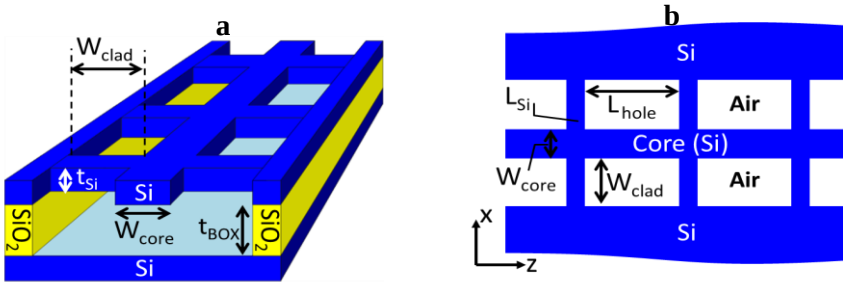

Fig. 1. Schematics of suspended waveguide with SWG lateral cladding: a) 3D view, b) 2D top view.

Fabrication constraints: The minimum feature size of our lithographic process is ~100 nm, On the other hand, the air holes should be larger than ~450×450 nm^2 to facilitate the flow of liquid HF through the SWG holes for BOX removal [9].

Waveguide mechanical stability: To assure the mechanical stability, the hole size should be minimized whereas the Si stripes must be robust enough to mechanically support the waveguide.

Optical properties: First, the SWG period Λ must be smaller than the Bragg period Λ_{Bragg} to ensure the devices operate in the subwavelength regime. We have estimated by simulations that $\Lambda_{Bragg} \sim 700$ nm, so that $\Lambda = L_{Si} + L_{hole} < 700$ nm. Since the lateral SWG cladding provides the refractive index contrast ($\Delta n = n_{Si} - n_{swg}$) required for waveguiding and the width of the SWG cladding (W_{clad}) should be minimized for structure mechanical integrity, a comparatively large refractive index contrast Δn is required to minimize lateral leakage. As can be seen in Fig. 2, this can be readily realized by choosing the width of the Si stripes to be substantially smaller than the size of air holes ($L_{Si} << L_{Hole}$). The influence of L_{Si} on the mode confinement can be observed in the insets of Fig. 2(a), which show the propagation of the fundamental mode in the suspended waveguide for two different SWG cladding geometries: $L_{Si} = 100$ nm (high Δn) and $L_{Si} = 225$ nm (low Δn). For the latter, a larger width W_{clad} of the lateral cladding is required to minimize lateral leakage.

Based on these considerations, the nominal waveguide geometry was selected as follows: the longitudinal SWG dimensions are $L_{Si} = 100$ nm and $L_{hole} = 450$ nm, as in ref [9], whilst the core width was increased to $W_{core} = 1.3$ µm to enhance the mode confinement in the Si core. This way the cladding width (W_{clad}) can be reduced without penalty on the lateral leakage of the fundamental mode. Following this strategy, we were able to substantially reduce the cladding width to $W_{clad} = 2.5$ µm, compared to 4 µm in [9], so that mechanical stability is significantly improved. The 1.3-µm-wide nominal waveguide also supports a second-order guided mode, albeit substantially delocalized and only weakly-guided [see Fig. 2(b)] with a large lateral leakage loss. Therefore, in terms of the light propagation characteristics the waveguide can effectively be considered as a single-mode structure.

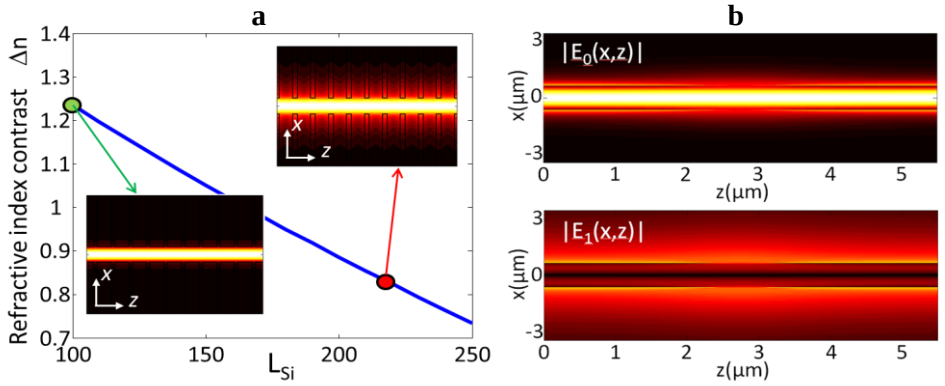

Fig. 2. (a) Refractive index contrast $\Delta n = n_{Si} - n_{swg}$ as a function of the length of the sustentation Si stripes L_{Si}. $W_{core} = 1.3$ µm, $L_{hole} = 450$ nm and $\lambda = 3.8$ µm. Insets: the fundamental mode propagation in the suspended waveguide for $L_{Si} = 100$ nm (left, high contrast) and $L_{Si} = 225$ nm (right, low contrast). (b) Calculated electric field of the fundamental Floquet-Bloch mode (top) and the second-order Floquet-Bloch mode (bottom) for $W_{core} = 1.3$ µm, $L_{hole} = 450$ nm, $L_{Si} = 100$ nm and $\lambda = 3.8$ µm.

In the next step of our design, we used this nominal waveguide geometry to implement S-bends and 90º bends [see Fig. 3]. To facilitate layout scripting, the supporting Si strips of the S-bend are oriented perpendicular to the longitudinal direction (z-axis). The waveguide path is defined as: $x = 0.5S\,[1\text{-}\cos(\pi z/L)]$, where L is the S-bend length and S is the lateral displacement. Since the desired adiabatic behaviour of the S-bend limits the maximum value of the bend angle θ [see Fig. 3(a)], the variations in the orientation of the Si stripes with respect to the light propagation direction along the bends is comparatively small. Simulation results show that the insertion losses are negligible for $\theta = arctan\,(\pi S/(2L)) < 15º$. For $S = 7$ µm and $\theta = 15º$,

the resulting S-bend length is L = 41 µm. For the 90º bend, the Si stripes are perpendicular to the light propagation direction, as shown in Fig. 3(b). The relation between the radius of curvature (R) and the angular discretization of the SWG ($\Delta\psi$) is: $R \approx \Lambda / \Delta\psi(\text{rad})$. We have determined, by simulations, that the 90º bend loss is negligible for radii >16 µm ($\Delta\psi \leq 2º$).

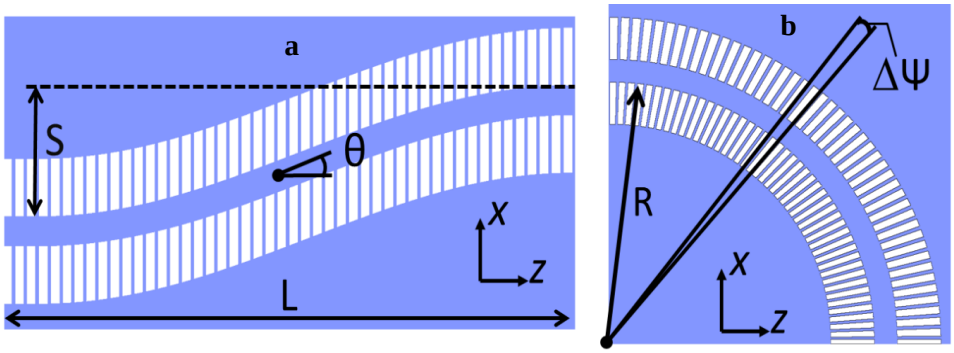

Fig. 3. Schematics of a suspended waveguide with a) an S-bend and b) a 90º bend.

2.2. MMI design

Multimode Interference (MMI) couplers are fundamental building blocks in photonic integrated circuits. MMIs are typically used as power splitters and combiners, often as part of more complex devices, such as Mach-Zehnder interferometers (MZIs), coherent receivers, or wavelength and mode multiplexers [14, 15, 16]. MMI advantages include compact size, comparatively large bandwidth, and relaxed fabrication tolerances. Since the MMI performance generally improves with decreasing the lateral index contrast [17, 18], using the SWG cladding reported in this work is expected to be beneficial for the overall MMI performance compared with a conventional MMI structures.

As a representative MMI example, we chose a 2×2 MMI with general interference mechanism [19] operating in TE polarization. A schematic 2D representation of the coupler is shown in Fig. 4. In order to optimize the MMI performance, we follow the general design approach described in [19]: First, the width of the access waveguides (W_A) is increased compared to the interconnecting waveguide width (as designed in section 2.1). Second, the access waveguide separation (W_S) is minimized while keeping the optical coupling between the input ports negligible. Then, the width (W_{MMI}) and the length (L_{MMI}) of the multimode section are optimized to simultaneously minimize the excess loss [$-10\log(|S_{31}|^2+|S_{41}|^2)$], power imbalance [$10\log(|S_{31}/S_{41}|^2)$] and phase error [$\text{phase}(S_{31}/S_{41})-90°$] at the output ports. Finally, linear tapers are designed to adiabatically connect the interconnecting waveguides with the access waveguide. Fig. 4 shows the MMI schematics, including optimized device dimensions and simulated field in the multimode section. Since the modal confinement is increased in the multimode section compared to the interconnecting waveguides, we narrow the SWG cladding width to 2 µm to improve mechanical stability, without noticeable penalty on the simulated optical performance.

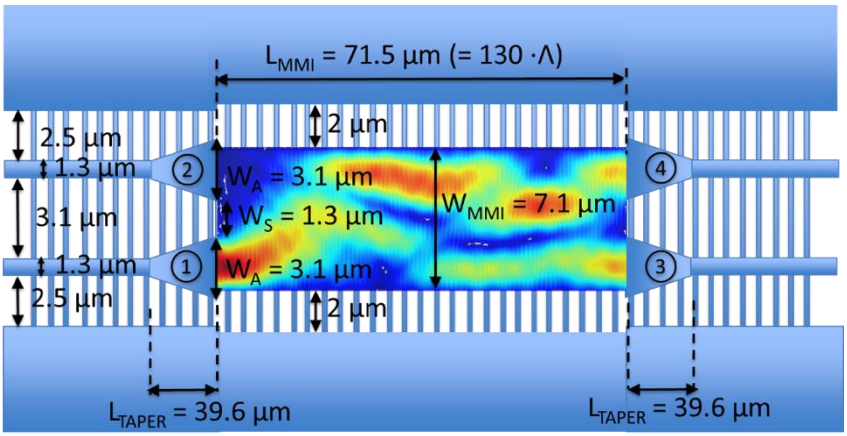

Fig. 4. MMI schematics and calculated electric field in the multimode section. Nominal device dimensions are also shown.

The overall MMI design performance is virtually perfect in the wide wavelength range of 3700 nm - 3900 nm, with minimal excess loss (<0.4 dB), imbalance (<0.15 dB) and phase errors (<2º). We also found that the MMI tolerates quite large deviations in width (ΔW= ±100 nm) and thickness (Δt_{Si} = ±60 nm), with the excess loss 1.3 dB, the imbalance 0.85 dB and the optical bandwidth 3750 nm - 3850 nm.

3. Device fabrication

The devices were patterned on a 6-inch SOI wafer, using a JEOL JBX 9300FS e-beam lithography tool with ZEP-520A as positive resist. A 4 nm spot size was utilized to improve sidewall roughness, which is an important parameter in our devices, due to the large sidewall surface in the SWG regions. Inductively coupled plasma reactive ion etching (ICP-RIE) with SF_6 and C_4F_8 chemistry was used to transfer the pattern to the silicon layer. Silicon etch rate in the SWG regions (with small holes) was found to be slower compared to that of conventional strip or rib waveguides (wider etching areas), therefore requiring a longer etch time which resulted in about 30 nm lateral over-etch. The chips were then dipped into a hydrofluoric acid (HF) bath to locally remove the BOX, resulting in the suspended structure. A 50 minute etch in 1:7 HF was required to completely remove the BOX underneath the widest structures (the MMIs width is 7.1 µm). This prolonged liquid HF bath produced a vertical and lateral Si over-etch of ~50 nm. In order to compensate for the combined ICP and HF lateral over-etches, a small positive bias of 40 nm per side (80 nm total) was applied to the length of the Si stripes (L_{Si}) in the SWG regions. No bias was applied to the core of the waveguide or the multimode region of the MMI.

The scanning electron microscope (SEM) images of fabricated devices [Fig. 5] show that the Si layer is fully etched and that the BOX is completely removed underneath the structures. Figures 5(a) and 5(b) show top views of a 90° bend an S-bend, respectively. Figure 5(c) shows two waveguides approaching the MMI region, while Fig 5(d) shows one half of the MMI. Figures 5(e) and 5(f) show cross-sections of suspended 90° bends and MMIs. An SEM image of a chip facet after BOX removal and cleaving steps is shown in Fig. 5(e). For the MMI device shown in Fig. 5(f), a focussed ion beam (FIB) has been used to etch an area across the centre of the multimode region, i.e. the structure with widest Si membrane. Cavity underneath the MMI device can also be observed in Fig. 5(f).

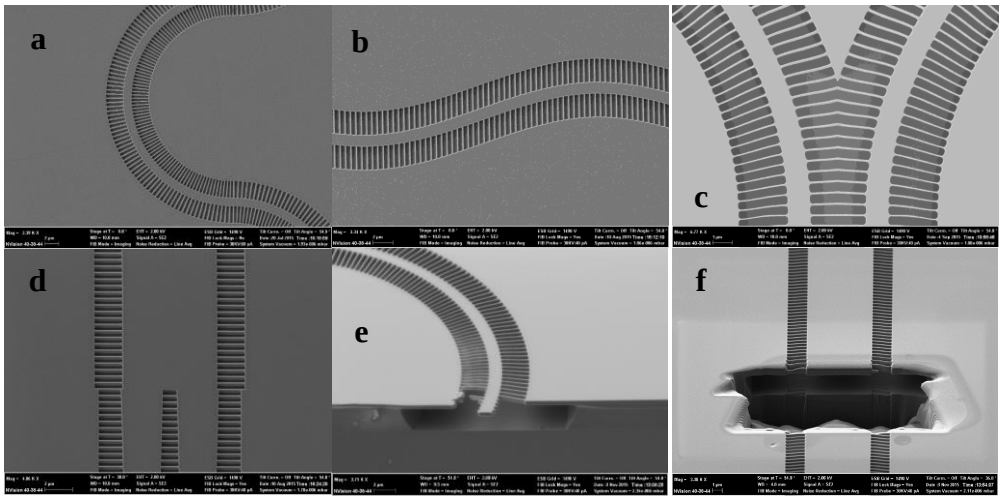

Fig. 5. SEM image of a) the 90º bend b) the s-bend c) waveguides converging towards the MMI input section and d) input section half of the MMI (top views). e) A cleaved facet of a 90º bend with the BOX locally removal, with a few destroyed silicon strips due to the cleaving. f) Under-etched multimode region of the MMI after FIB cut, with no appreciable deformation of the suspended structure.

4. Measurement results

TE polarized light from a tuneable quantum cascade laser operating at 3.8 µm wavelength was coupled in and out the chips using subwavelength engineered surface grating couplers [20, 21]. Detail description of our experimental setup can be found in ref. [12]. The measured propagation loss for the suspended waveguide with nominal dimensions W_{core} = 1.3µm and W_{clad} = 2.5µm is 0.82 dB/cm. This loss is comparable to state of the art strip waveguides for this wavelength [21] and substantially smaller compared to the suspended waveguides used in our previous work (W_{core} ~ 1.1µm, W_{clad} = 4µm, loss 3.4 dB/cm) [9]. This significant loss reduction is mainly due to two factors: i) the increased core width, which reduces the interaction of the modal field with the lateral core/cladding interface and ii) an improved fabrication technique (4 nm e-beam spot size, compared to 20 nm in [9]) which reduces sidewall roughness. The measured propagation losses are shown in Figure 6(a), before and after HF under-etching.

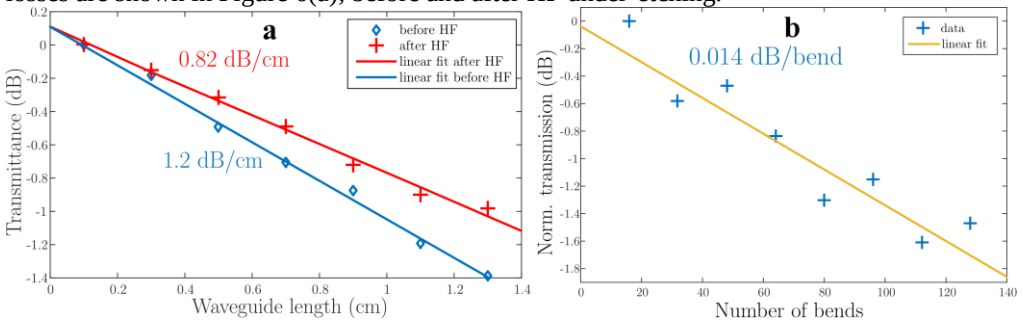

Fig. 6. a): Waveguide propagation loss measurement before and after HF etching. The results are normalized to the transmission measured for the shortest waveguide (0.1 cm). The blue line is a linear fit to the measured data (diamond symbols) before HF etching (1.2 dB/cm). The red line is a linear fit to the measured data (cross symbols) after HF etching (0.82 dB/cm). b): Linear fit (yellow line) to the 90º bend loss measurements (cross symbols) after HF etching (0.014 dB/cm).

The loss reduction achieved with the suspended structure is modest (~0.4 dB/cm), since the mode field is mostly confined within the Si core and the SiO_2 material losses are not yet prohibitive at 3.8 µm wavelength. As such, we have not yet exploited the full potential of suspended structures for mid-IR applications. The advantage of our SWG waveguides indeed

would become even more prominent for longer wavelengths (4µm - 8µm) where the SiO_2 absorption loss increases dramatically. For our waveguide bend structures, the loss is well below 0.02 dB, specifically 0.014 dB/bend for 90º bends with radius of 15.7 µm [Fig. 6(b)] and 0.01 dB/bend for S-bends with 41 µm length and 7 µm offset.

The MMI measurement results are shown in Fig. 7(a). The excess loss and imbalance are below 1.6 dB and 0.5 dB, respectively, in the wavelength range of 3720 nm - 3800 nm, with a noticeable performance penalty compared to the simulation results (0.4 dB excess loss and 0.15 dB imbalance). This penalty can be attributed to the aforementioned reduction in both the thickness and width of silicon layer during the fabrication process. To verify this, we carried out several simulations combining different reductions in both the thickness and width of the nominal device dimensions. We find that there is a good agreement between the experimental results and calculations when the influence of a -80 nm fabrication error is included in the simulation, as can be observed in Fig. 7(a).

We have also characterized an asymmetric Mach-Zehnder Interferometer (MZI) incorporating our 2×2 MMIs. The length imbalance between both MZI arms is $\Delta L = 350$ µm, yielding a measured Free Spectral Range (FSR) of ~9.6 nm [see Fig. 7]. The measured group index is $n_g = \lambda^2/(\Delta L \cdot FSR) \sim 4.2$, in good agreement with our simulations. Both MZI outputs are almost perfectly interlaced, implying that MMI phase error is low. The measured extinction ratio at the worse output is ~15 dB. From this value we estimate that the power imbalance of the MMIs is less than 0.7 dB.

All data supporting this study are openly available from the University of Southampton repository at http://dx.doi.org/10.5258/SOTON/397394.

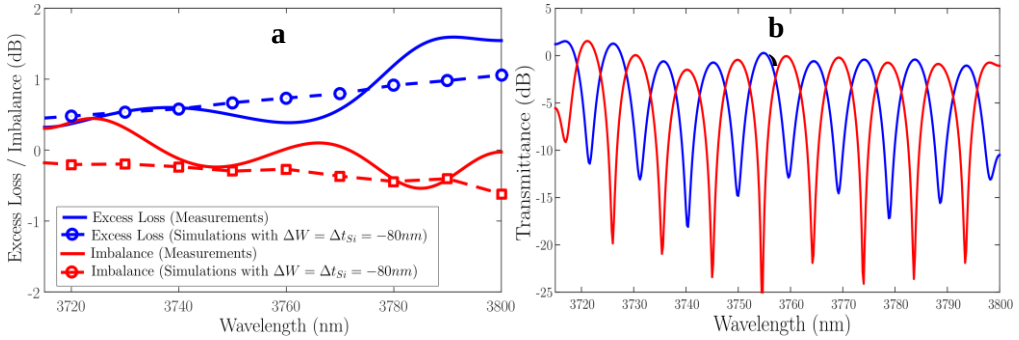

Fig. 7. a) Measured MMI insertion loss (solid blue line) and imbalance (solid red line). The dashed lines show calculated excess loss and imbalance taking into account a fabrication error of -80 nm in Si waveguide core width and thickness. b) Measured MZI transmittance for both outputs, with an FSR of 9.6 nm and an extinction ratio exceeding 15 dB.

5. Conclusions

We have demonstrated a set of suspended MIR silicon SWG engineered devices, such as waveguides, bends, MMI couplers and Mach-Zehnder interferometers. The measured waveguides propagation loss is 0.82 dB/cm, one of the lowest values yet reported for the mid-infrared waveguides. Also, it is for the first time that functional devices such as MMIs and MZIs were demonstrate in this new MIR platform. Such devices are of fundamental importance for building mid-IR photonic integrated circuits. These results demonstrate an excellent potential of the subwavelength grating engineered devices for the mid-infrared, potentially extending the wavelength range of the SOI platform to the entire transparency window of silicon.

6. Funding

EPSRC MIGRATION (EP/ L01162X/1); Ministerio de Economía y Competitividad (MINECO) Programa Estatal de Investigación, Desarrollo e Innovación Orientada a los Retos de la Sociedad (cofinanciado FEDER) (TEC2013-46917-C2-1-R).

7. Acknowledgements

G. Z. Mashanovich would like to acknowledge support from the Royal Society through his University Research Fellowship (UF120053).